Meas. Sci. Technol. **18** (2007) 3751–3767 doi:10.1088/0957-0233/18/12/010

# Three-dimensional reconstruction of specular surface for a gas tungsten arc weld pool

**Hong Sheng Song and Yu Ming Zhang**

Center for Manufacturing and Department of Electrical and Computer Engineering, University of Kentucky, Lexington, KY 40506, USA

E-mail: ymzhang@enrg.uky.edu

Received 14 March 2007, in final form 16 July 2007
Published 19 October 2007
Online at stacks.iop.org/MST/18/3751

**Abstract**

Observing the weld pool and measuring its geometrical parameters are key issues for developing the next generation intelligent welding machine and modeling the complex welding process. In the past few years, different techniques have been applied, but the dynamic specular weld pool surface and the strong weld arc complicate these approaches and make observation difficult. To resolve the problem, a new three-dimensional sensing system using structured light is proposed for a gas tungsten arc welding (GTAW) process. In the system, a dot-matrix laser pattern is projected on the specular weld pool surface, which can reflect light onto an imaging plane. The reflected images are captured by a high-speed camera and can successfully be processed by image processing algorithms developed. With the acquired information, a three-dimensional reconstruction scheme is proposed and discussed in this paper. A surface reconstruction method with several slope-based algorithms is first developed to rebuild the region of weld pool surface which reflects the laser pattern. Then a two-dimensional piecewise model is provided to calculate weld pool boundary by utilizing the edge condition. Finally the optimal estimate of the three-dimensional weld pool surface is synthesized. The acceptable accuracy of the results verified the effectiveness of the reconstruction scheme.

**Keywords:** weld pool, surface, pool surface, specular surface, specular reflection, three-dimensional, measurement, monitoring, welding, GTAW

(Some figures in this article are in colour only in the electronic version)

## List of notation and definitions

*Base point (points).* The reflection point (points), whose position(s) is (are) assumed and used to calculate the positions of other reflection points as a base, is (are) called base point(s).

*Column plane.* For a point $p_{i,j}$ located in the $i$th row and the $j$th column of the projected dot matrix, the plane passing through all the dots in the $j$th column and the dot of laser diode is called the column plane of point $p_{i,j}$.

*Center reference point.* The center point in the projected dot matrix of structured light. For a 19-by-19 dot matrix, it is located in the 10th row and the 10th column. It is not an actual visible point but a reference position, which can be used to find the corresponding relationship between projected and reflected points.

*GTAW.* Gas tungsten arc welding

*Normal.* A normal to a flat surface is a three-dimensional vector which is perpendicular to that surface, and a normal to a non-flat surface at a point P on the surface is a vector which is perpendicular to the tangent plane to that surface at $P$.

*Reflected dots (points).* The dots reflected on the imaging plane.

*Reflected image.* The captured image including the reflected dots on the imaging plane.

*Reflection dots (points).* The dots projected on the weld pool surface, also called projected dots.

Row plane. For a point $p_{i,j}$ located in the $i$th row and the $j$th column of the projected dot matrix, the plane passing through all the dots in the $i$th row and the dot of laser diode is called the row plane of point $p_{i,j}$.

*Tangent plane.* $P$ is a point on the surface $S$. If the tangent lines at $P$ to all smooth curves on the surface $S$ passing through $P$ lie on a common plane, then that plane is called the tangent plane to surface $S$ at point $P$.

*Three-dimensional (3D) slope.* The tangent plane of a point $P$ on a surface $S$ is also called the 3D slope of the point $P$.

*Two-dimensional (2D) slope.* $P$ is a point on the surface $S$ and a plane $T$ passing point $P$ intercepts surface $S$ to produce a curve. The tangent line of the curve at $P$ is called the 2D slope of point $P$ on surface $S$ along the plane $T$.

## 1. Introduction

Welding is a labor intensive operation and automation is a major way to assure and help improve its productivity and quality. However, welding is also an operation which requires high skills especially for critical applications. While current welding robots can provide consistent motion to help assure productivity and quality, they lack the level of intelligence/judgment capabilities that skilled human welders possess. Being more intelligent is the ultimate direction for next generation automated welding machines. Since skilled human welders can only concentrate on observing the weld pool (surface) (but they can still make quality welds as long as they can maintain their concentration!), the weld pool surface must contain sufficient information about the weld quality. In addition, the weld pool surface can help better observe and understand the complex welding process/phenomena and provide critical experimental data to validate numerical models of welding processes. Hence, the measurement of the three-dimensional weld pool surface is a fundamental capability that next generation automated welding machines and welding researchers must possess, and a number of early efforts have been devoted to sense weld pool related parameters using a few methods including machine vision, x-radiation, ultrasonic and acoustic emission, etc [1–4].

Among existing methods, vision-based ones have been studied more extensively. In vision-based methods, vision-based sensors acquire images from the weld pool and image processing is followed to analyze and extract weld pool related parameters so that control algorithms can use these parameters as feedback to adjust welding parameters [5–7]. Early work on vision sensor based direct view of weld pool has been done in the Welding Research Laboratory at the University of Kentucky using a specially designed commercial camera whose high speed shutter is synchronized with a short duration pulsed laser [5]. This camera allows the arc light to be eliminated from the image to acquire an image shown in figure 1(*a*). As a result, the two-dimensional boundary of the weld pool is clearly imaged. To use this camera in three-dimensional weld pool surface imaging, a special technique was used which projected the structured illumination laser through frosted glass [6]. As a result, an image as shown in figure 1(*b*) can be acquired [6]. In a separate effort, Mnich and his colleagues used a stereovision method to determine the three-dimensional shape of the weld pool [7]. Another effort used a similar principle but introduced the biprism technique to reduce the number of needed cameras from two to one [8]. While all these methods have achieved a certain success, the welding community clearly requires methods which are more robust, accurate, cost effective and suitable for the welding environment. For example, although the special camera with laser-shutter synchronization can acquire beautiful images using frosted glass as in figure 1(*b*), the system is extremely expensive and can only reach 30 frames per second because it uses a pulsed illumination laser to suppress the arc light while the average power of the illumination laser is relatively low. Because the weld pool surface is highly dynamic, acquiring useful information on the weld pool surface requires a much higher imaging frame rate.

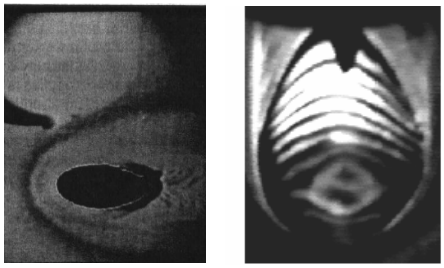


**Figure 1.** Captured images for (*a*) 2D measurement [5] and (*b*) 3D measurement [6].

The authors have proposed a different approach to observing the weld pool surface [9, 10]. It projects a low-power continuous structured pattern of laser beams onto the weld pool surface and intercepts the reflection of the projected laser from the specular weld pool surface. Because the welding arc radiation decays very fast with the travel distance while the reflection of the projected laser remains almost constant in intensity, it is possible that the reflection of the projected laser can be clearly imaged on the interception plane. Because the imaging on the interception plane is continuous, the imaging speed is only affected by the frame rate of the camera used. This proposed method appears to be more cost effective, convenient, robust and suitable for manufacturing applications due to the use of a continuous low power laser. However, although the formation of the image is governed by the reflection law, the image itself does not provide an intuitive view about the dimensions of the weld pool surface. Reconstruction algorithms are needed to derive the three-dimensional shape of the weld pool surface by solving an inverse problem of the reflection law. Hence, in this paper, a reconstruction scheme with two slope-based algorithms and a two-dimensional piecewise boundary model is developed. The reconstructed results show the validity of the proposed scheme. One thing should be mentioned here. In this study, the projected laser pattern is a 19-by-19 dot matrix instead of the 5-line pattern previously used in [9, 10] because dot light (ray) is easier to track based on the reflection law and this simplifies the reconstruction.

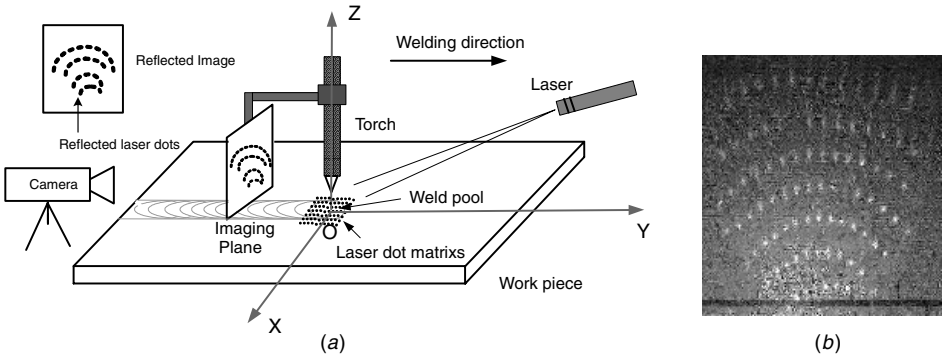


**Figure 2.** Sensing system: (*a*) system diagram and (*b*) one captured image.

The paper is organized as follow. Section 2 introduces the processes used for generating the reconstruction data, in which the proposed measurement system as well as the correspondence simulations and image processing algorithms are shown. Then the main idea of the developed reconstruction scheme is discussed in section 3, and the included three-dimensional surface reconstruction method and boundary modeling are described, respectively, in sections 4 and 5. In sections 6 and 7, the realization of the reconstruction scheme and the experimental results are presented. Finally, the findings and conclusions are summarized in section 8.

## 2. Generation of reconstruction data

Before the weld pool surface is reconstructed, a sensing system is proposed to image the laser rays reflected from the weld pool surface. To match each reflected ray/point to its incident ray, correlation analysis is done through simulation. Based on the simulation results and the results of reflected image processing, such as the row–column relationship of the reflected points and the position of the center reference point, pairs of reflected point and incident ray can be obtained to reconstruct the weld pool surface which can be used to recalculate the reflected points from the incident rays.

### *2.1. Sensing system*

The proposed weld pool surface sensing system is shown in figure 2(*a*) [10]. The welding process used in the system is gas tungsten arc welding (GTAW), the primary arc welding process for precision joining of metals. To observe the three-dimensional weld pool surface, a 20 mW illumination laser at a wavelength of 685 nm with variable focus is used to generate a 19-by-19 dot-matrix structured light pattern. The laser pattern is projected onto the area under the torch electrode and covers the whole possible weld pool surface. During the welding process, the molten specular weld pool surface is just like a mirror and it can reflect the majority of the incident laser light. In order to intercept the reflected laser pattern, an imaging plane is placed at a distance of about 50 mm from the electrode. It can be as simple as a piece of glass attached with a grid paper. In the meantime, a high-speed camera is used to record the reflected images on the imaging plane. To minimize the influence of the arc, the camera is fitted with a band pass filter of 20 nm bandwidth centered at a wavelength of 685 nm. As shown in figure 2(*a*), a universal coordinate system is established in order to locate the positions for all the objects in the sensing system. In the system, the torch is on the *Z*-axis and the work piece is in the *X*–*Y* plane.

Figure 2(*b*) shows a reflected image acquired in one experiment by projecting a 19-by-19 dot-matrix pattern with an inter-beam angle 0.77°, on which the laser dots have been shaped by the weld pool surface and the straight rows in the projected dot pattern have been changed to convex curves. In this experiment, a sheet of 2 mm thick mild steel is used as the work piece and the welding current is kept at 75 A with the constant welding speed of 3 mm $s^{-1}$. Although as can be seen from figure 2(*a*), the area covered by the laser pattern is larger than the weld pool area, only the dots projected on the weld pool surface can be reflected onto the imaging plane. The intensity of the reflected dots and the contrast of the acquired image are a little low, but as will be shown later the reflected image can still be processed to extract the reflected dots for analysis. Hence, a higher laser power is not a must.

### *2.2. Correspondence simulation*

As can be seen from figure 2(*b*), the similarity of the reflected dots in the captured image makes it difficult to tell which incident rays in the dot matrix they come from. Simulation is thus conducted in order to find the possible correspondences between projected and reflected laser points.

The point position can be recognized by its row and column numbers not only for the projected dot matrix but also for the reflected image. Figure 3 uses a 7-by-7 projected dot matrix as an illustration example. This example will also be used later in this paper to illustrate the reconstruction scheme. In figure 3(*a*), $p_{i,j}\,(1 \leqslant i, j \leqslant 7)$ represents the projected point in the *i*th row and *j*th column. A possible reflected dot pattern similar to the one on the captured image is shown in figure 3(*b*). The reflected row and column are distorted by the weld pool surface, and $r_{i,j}$ represents the reflected point in the *i*th row and *j*th column. As can be seen, the number/position of reflected dots depends on the size/shape of the reflection surface and different rows may have different numbers of reflected dots. For example, there are three reflected dots in the first row and five in the second row.

In the simulation, two kinds of corresponding relationships in the dot-matrix pattern are considered as shown in figure 4. One is the column correspondence, which

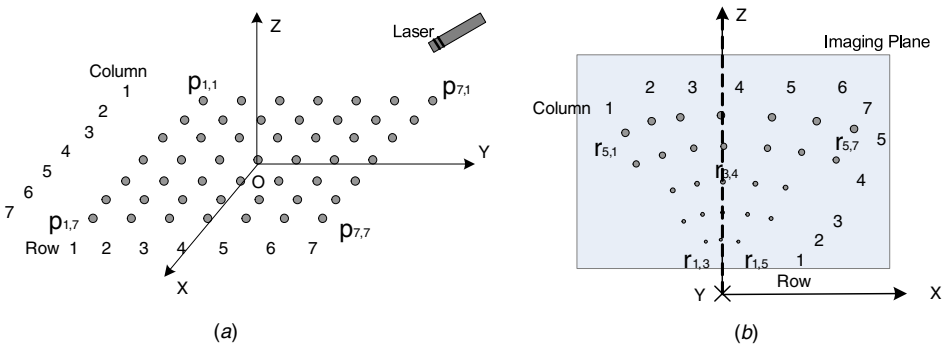


**Figure 3.** Projected and reflected dots locating (*a*) projected dot matrix on the *X*–*Y* plane and (*b*) reflected dot pattern on the imaging plane.

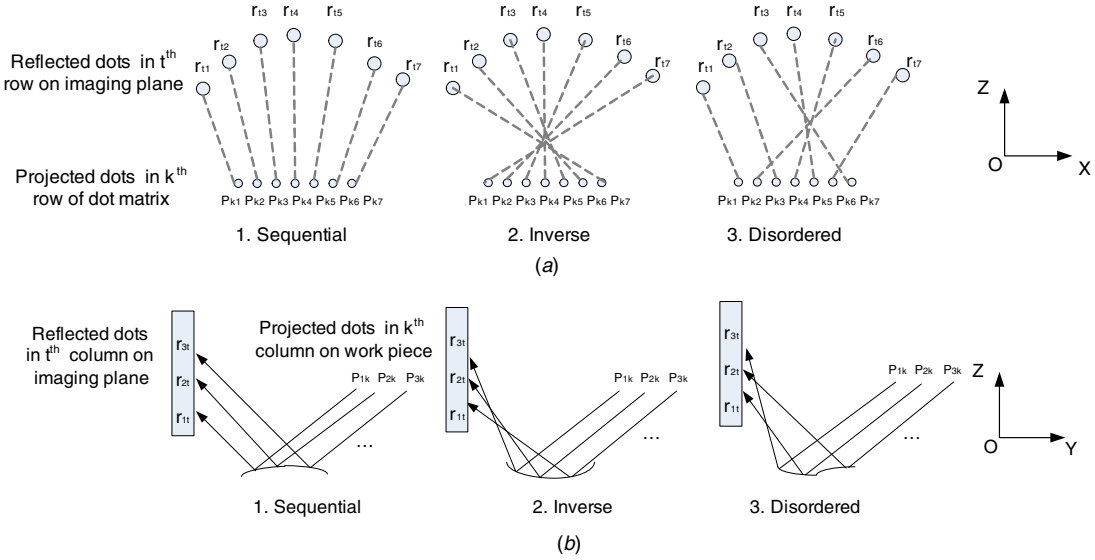


**Figure 4.** Illustration of two kinds of corresponding relationships: (*a*) column corresponding relationship and (*b*) row corresponding relationship.

represents the column relationship of dots in a projected row and its reflected row. The other is the row correspondence, which tells the row relationship of dots in a projected column and its reflected column. They both have three types of mapping according to different shapes of reflection surface: sequential, inverse and disordered. In figure 4(*a*), the dots in the *k*th row of the projected dot matrix are investigated and the dashed lines indicate the column corresponding relationship between the projected and reflected points. In figure 4(*b*), three types of mappings of column corresponding relationships are shown. As can be seen, the differences among these mappings are caused by different statuses of the weld pool surface, such as shallow/deep and concave/convex.

Based on the assumption of small deformation in the smooth weld pool surface, a part of a sphere is tested as a simple concave/convex weld pool surface in the simulation [11]. System position parameters are set according to our experiments and the dimension of simulated surface is set within the practical range for GTAW. First different sizes of weld pool are investigated and the width/length of the weld pool is changed from 4 mm to 10 mm. Secondly the depth of weld pool surface is changed from 1/100 to 1/10 of its width. The simulations show that for most simulated concave surfaces, the shape of the reflected dots in a row is convex just as shown in figure 4(*a*) and the row and column corresponding relationships are inverse. Here 'convex' means that if the reflected dots in a row are connected, the shape of the curve is convex. But for some cases when depth is very small, the row's corresponding relationship is inverse and the column's is sequential. If the simplified convex surfaces are used in the simulation, the row and column corresponding relationships are all sequential and the shape of the reflected dots in a row is also convex.

### 2.3. *Processing of reflected image*

The acceptable clearness of the captured images from the proposed approach assures that they can be processed to accurately extract the laser dots shaped by the specular weld pool surface and thus be used to accurately compute the weld pool surface. The flowchart of the developed reflected image processing scheme is shown in figure 5 [11].

In the scheme, first the reflected laser points in the image are extracted based on their shape and size, and some image processing techniques are used, such as blocking threshold segmentation method [12], median filter and morphological operations [13]. Following the proposed procedures, the original reflected image in figure 6(*a*) is processed and the

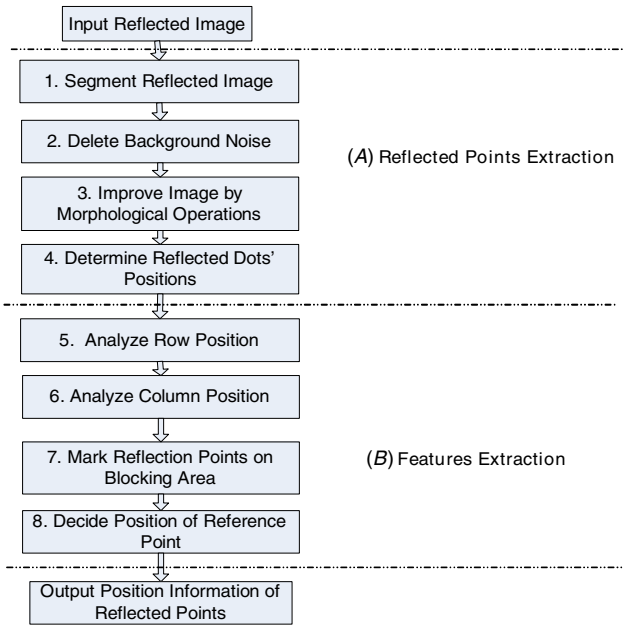


**Figure 5.** Flowchart of image processing.

result is shown in figure 6(*b*). As can be seen, the proposed dot extracting algorithm is capable of extracting the reflection points from the image with reduced contrast. One thing that should be mentioned here is the positions of reflected dots using imaging plane coordinates shown in figures 6(*a*) and (*b*), can be converted into universal coordinates by using system position parameters.

After the extraction of the reflected dots, their positions are analyzed and some image features are determined [11], such as the row–column relationship and the corresponding position of the center reference point. Here the row–column relationship means the row and column positions of reflected dots on the imaging plane, which is shown in figure 3(*b*). In figure 6(*c*), it can be seen that the center point $p_{10,10}$ (in the 10th row and 10th column) in the projected 19-by-19 dot matrix is intentionally made absent. This property can ease the matching of reflected dots and $p_{10,10}$ is defined as 'center reference point' although it does not actually exist. In figure 6(*b*), 7 rows and 16 columns of reflected dots are recognized by the proposed feature extracting algorithm and the corresponding position of the center reference point $r_{6,7}$ is also easily decided in the 6th row and 7th column, which is only referring to a position not an actual point.

Finally, the results of correspondence simulation in section 2.2 can be further applied to match the reflected points to their projected rays based on the features extracted by the reflected image processing. Suppose $R = \{r_{i,j}, (i, j) \in I\}$ represents the set of reflected dots on the imaging plane $I$ and $P = \{p_{i,j}, (i, j) \in S\}$ represents the set of corresponding projected (reflection) dots on the weld pool surface $S$ (here the subscripts represent the row and column positions of the dots and the numbers of dots in sets $P$ and $R$ are the same), if the corresponding position of the center reference point $p_{10,10}$ on the reflected image is $r_{r,c}$, the corresponding relationships between reflected dots and projected dots can be expressed as follows.

- For sequential row and column corresponding relationships $r_{i,j} \xleftrightarrow{\text{reflection}} p_{i-r+10,\,j-c+10}$.
- For inverse row and column corresponding relationships $r_{i,j} \xleftrightarrow{\text{reflection}} p_{r-i+10,\,c-j+10}$.

Together with the corresponding relationship discussed in section 2.2 and features found in section 2.3, each reflected dot on the imaging plane can be successfully matched with a projected dot in the matrix for each possible row/column corresponding relationship. The matched point–ray pairs are now used to reconstruct the weld pool surface below.

## 3. Reconstruction scheme

After acquiring the necessary data and system position parameters for reconstruction, the reconstruction problem can be restated. Every incident ray in the projection laser dot-matrix can be represented by a line equation with the knowledge of the laser position and angle. In figure 7, LA is one of the laser rays in the projection dot-matrix and the equation of line LA is known. This ray is reflected by an unknown specular surface $S$ to produce a reflected point $R$ on the imaging plane. Then the objective of the reconstruction is to acquire the intersection (reflection) point $P$ of the incident line LA and the reflected line BR on the surface $S$. It is apparent

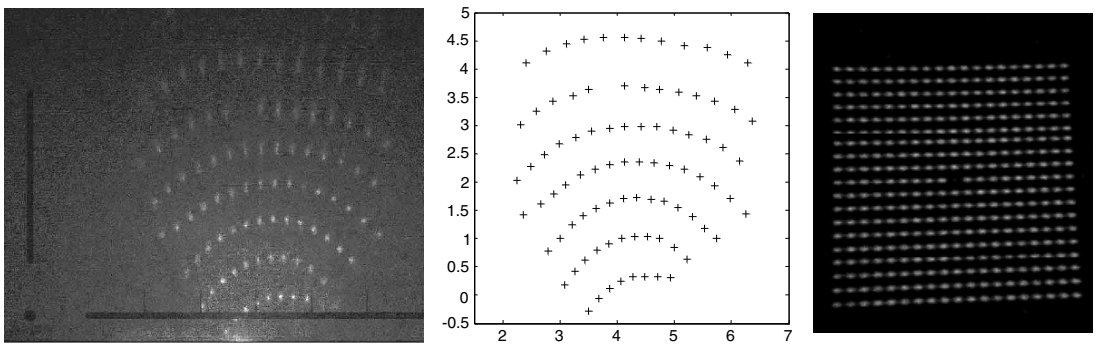


(*a*) (*b*) (*c*)

**Figure 6.** Reflected image processing: (*a*) original reflected image; (*b*) extracted reflected dots; and (*c*) vertically projected dot matrix.

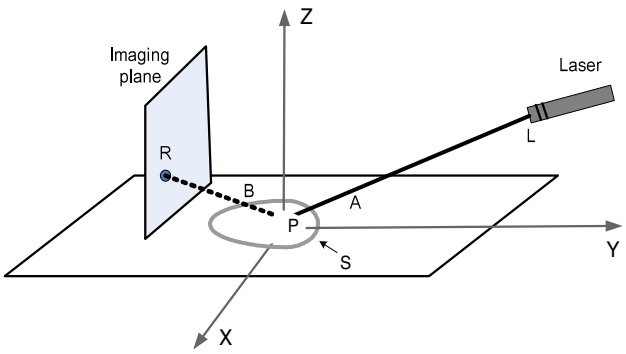


**Figure 7.** Problem illustration.

that the reflection point $P$ cannot be calculated directly because of insufficient constraints. To resolve this issue, an engineering method should be proposed to estimate the position of the reflection point $P$. Since there is a dot matrix projected on the surface, the positions of a series of reflection dots on the surface can also be optimally estimated, which will be used to reconstruct the surface $S$ as the three-dimensional weld pool surface.

In the experiments using mild steel as work pieces, two important facts have been observed and confirmed. The first is that the dots projected within the weld pool area will be reflected by its specular surface and others located out of the weld pool will not be reflected. This means all the dots on the captured image are reflected from the weld pool surface. The second is that the incident laser dot and its reflected dot on the imaging plane can easily be matched by locating the center reference point and finding the corresponding relationship as mentioned in section 2.

Based on the problem statement and two facts discussed above, an iteration process is proposed as the surface reconstruction method.

(0) Assume a surface as the initial estimate of the weld pool surface.
(1) Use the estimated surface, the reflection points on the surface which reflect the incident rays and the reflection rays can thus be calculated as estimates.
(2) The calculated reflection rays and their matched incident rays can be used to calculate a field of slopes at reflection points based on the reflection law.
(3) The field of slopes can be used to calculate a new surface as the updated estimate of the weld pool surface.
(4) Using the updated surface and the incident rays, the new reflected image can be calculated. The differences between the reflected points in the acquired and calculated images can be further mapped into the errors of reflection points on the weld pool surface. If this error meets the preset threshold, the updated surface is accepted as the weld pool surface; otherwise the updated surface is used as a new initial surface to repeat the iteration process starting from step (1).

In particular, since the depth of the weld pool is much smaller than its width and length for the GTAW process [14], it is reasonable to use a flat plane, i.e., $Z = 0$, as the initial estimate of the weld pool surface in step 0. To use the slope field to estimate dots on the weld pool surface, the weld pool surface is assumed to be smooth. With known dots on the weld pool surface, a new surface can be re-estimated/reconstructed using surface fitting or interpolation methods. Since it is difficult to set up a proper three-dimensional model for a weld pool surface, interpolation is adopted in the proposed scheme.

In addition, in order to get the surface boundary information which cannot be gained from the interpolation a two-dimensional boundary model is introduced as part of the proposed reconstruction scheme and the whole weld pool surface can thus be reconstructed.

## 4. Slope-based surface reconstruction method

Figure 8 shows the flow chart for a slope-based reconstruction method proposed to reconstruct/estimate a surface from a given field of slopes. It requires system parameters and processed reflected image as well as the corresponding relationship as inputs. As can be seen, the basic idea of the method is using slope information to compute/update the reflection points on the pool surface and interpolate the surface based on the updated reflection points. Here two different algorithms have been proposed to compute the updated reflection points from a given slope field: edge-point algorithm (EPA) and one-point algorithm (OPA).

Under the assumption of one possible corresponding relationship, the projected (reflection) dot set $P$ on the weld pool surface and its corresponding reflected dot set $R$ on the imaging plane can be decided. As discussed in section 2.3, they can be presented as $P = \{p_{i,j}, (i, j) \in S\}$ and $R = \{r_{i,j}, (i, j) \in I\}$. Here $S$ and $I$ represent the weld pool surface and imaging plane, respectively. The steps of the algorithm are described in detail as follows.

*Step* 0: a flat plane ($Z = 0$) is used as the initial estimate of the weld pool surface.
*Step* 1: use the assumed surface to compute the slope field.

The estimate of the weld pool surface, or the initial estimate $Z = 0$ plane for the first time, is used to calculate the positions of the estimated reflection dots $p'_{i,j}$ in the set $P'$ ($P' = \{p'_{i,j}, (i, j) \in S\}$) and thus all the reflected lines. By using the reflection law, the normal of every reflection point $p'_{i,j}$ on the surface can be computed from the corresponding incident and reflection line equations. Then the tangent plane at the reflection dot $p'_{i,j}$ can be computed, which is referred to as its 3D slope. This tangent plane intersects with the row plane and the column plane of dot $p'_{i,j}$. The resultant intersection lines are the two tangent lines along the planes, and the 3D slope is decomposed into two 2D slopes: horizontal row and vertical column slopes. Thus the slope field of the surface at different reflection points is formed. The definitions of normal, tangent plane, row plane, column plane, 3D slope and 2D slope can be found in the section 'List of notation and definitions'.

The 7-by-7 dot matrix in figure 3 is also shown as an example of slope computation in figure 9. Suppose point $p'_{4,4}$ is a point on the assumed surface S of the weld pool. Based on the reflection law, it is easy to obtain its normal line and tangent plane $K$. The 3D slope at the point $p'_{4,4}$ can be decomposed into row slope and column slope, by intersecting

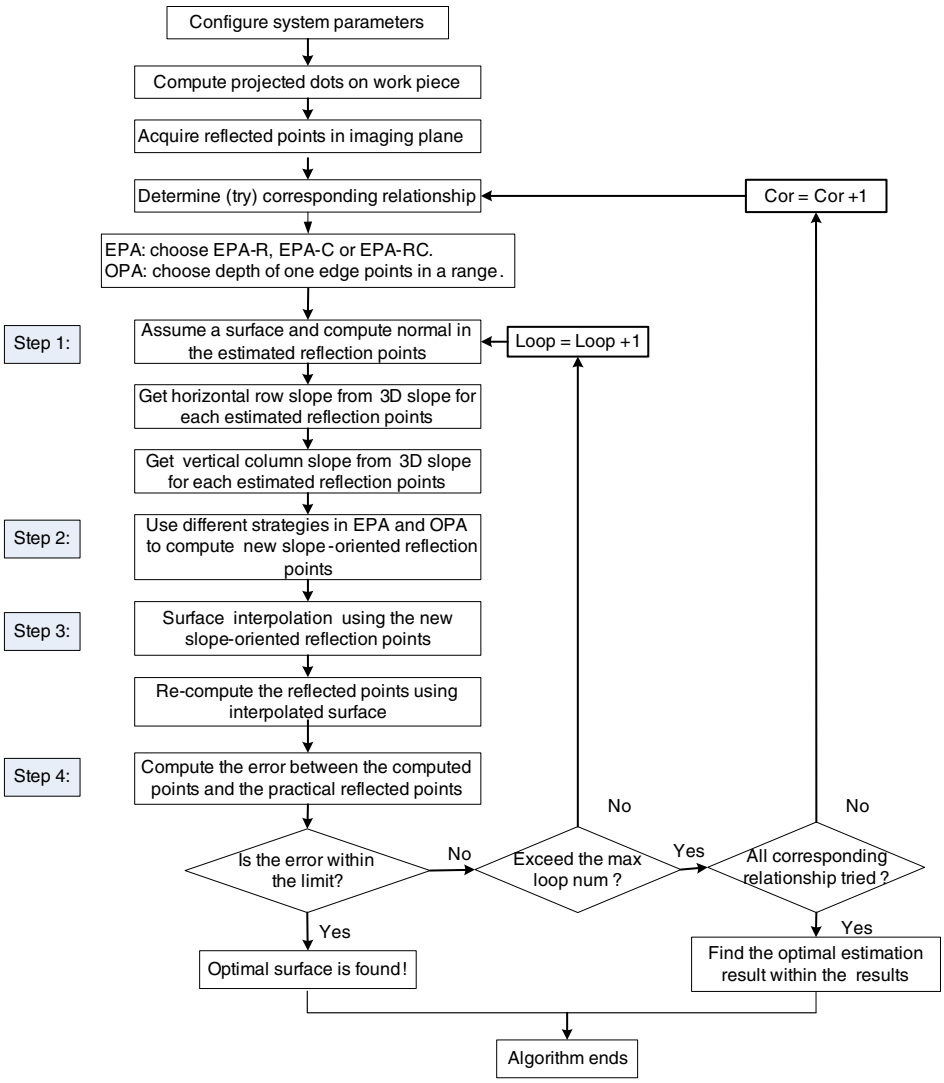


**Figure 8.** Flow chart of the slope-based surface reconstruction method.

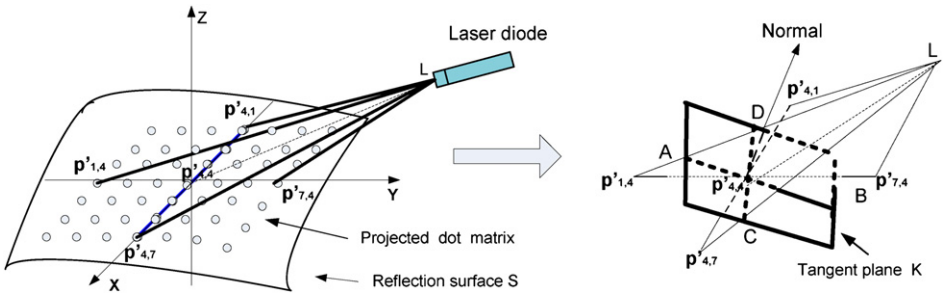


**Figure 9.** 3D slope decomposed into two 2D slopes.

its row plane $Lp'_{4,1}p'_{4,7}$ and column plane $Lp'_{1,4}p'_{7,4}$ with the plane $K$. As can be seen in figure 9, lines AB and CD are the resultant intersections and are thus the two 2D tangent lines. Their slopes in planes $Lp'_{4,1}p'_{4,7}$ and $Lp'_{1,4}p'_{7,4}$ are the two 2D slopes of point $p'_{4,4}$ in the vertical and horizontal direction, respectively.

*Step* 2: compute the new slope-oriented reflection points based on the slope field.

Since the shape of the weld pool surface is shallow, it is reasonable to take the computed slopes at estimated $P'$ as the slopes of the actual reflection points $P$ on the weld pool surface. Since the estimated surface in the first step cannot meet the slope requirements to produce the reflected image, the positions of new slope-oriented reflection point set $P''$ ($P'' = \{p''_{i,j}, (i, j) \in S\}$) are calculated by using these estimates of slopes in the second step.

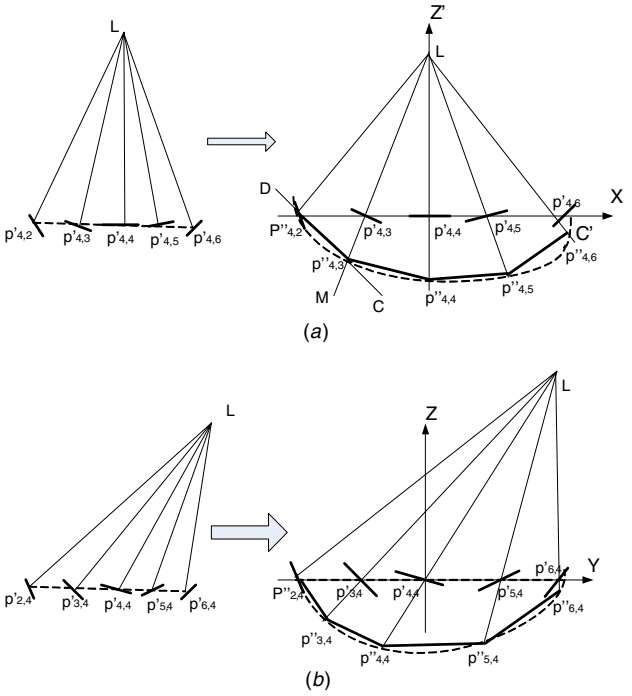


**Figure 10.** Computation of slope-oriented points: (*a*) row plane of point $p'_{4,4}$ and (*b*) column plane of point $p'_{4,4}$.

The position of slope-oriented reflection point $p''_{i,j}$ can be determined by either estimated row slopes in its row plane or column slopes in its column plane. Here the same example in figure 3 is taken and sequential row and column corresponding relationships are assumed. Suppose the reflected image is obtained as figure 3(*b*) and the corresponding projected point of reflected point $r_{3,4}$ is $p'_{4,4}$. The row plane/column plane of point $p'_{4,4}$ and the computed 2D slopes of the reflection points in its row/column are presented in figure 10 . As can be seen, different 2D coordinate systems are taken in the row/column plane with regard to the computed row/column slopes.

In figure 10(*a*), the row slopes of the points in the 4th row on the assumed surface have been computed in the first step. If the weld pool surface is flat, these slopes must be zero. Non-zero slopes indicate that these points on a flat surface should be replaced by better estimates of slope-oriented reflection points located on their incident rays and the new estimates $p''_{i,j}$ should be so determined that they can better meet the constraints given by the slopes. To obtain the new slope-oriented points ($p''_{4,3}$, $p''_{4,4}$, $p''_{4,5}$ and $p''_{4,6}$), select the edge point $p''_{4,2}$ as a base point. In order to find the position of $p''_{4,3}$, the directions of line CD should be found first, then $p''_{4,3}$ can be got as the intersection points of the incident ray LM and the line CD since the reflection point on the weld pool surface must also be on its incident ray. In order to simplify the computation, the line direction of adjacent points is set to be the average value of the two points' row slopes under the assumption of a dense projected dot matrix. For instance, the direction of CD can be computed as equation (1).

$$S_{CD} = \left(S_{p'_{4,2}} + S_{p'_{4,3}}\right)/2 \tag{1}$$

where $S_{p'_{4,2}}$ and $S_{p'_{4,3}}$ represent the row slopes of point $p'_{4,2}$ and $p'_{4,3}$, respectively. Following the same procedures, the other slope-oriented reflection points in the same row are computed and the dashed curve in figure 10(*a*) indicates the possible profile of the weld pool surface. In the same way, the column slopes can also be used to compute the new slope-oriented reflection points as shown in figure 10(*b*).

As can be seen, the positions of slope-oriented reflection points are measured in relation to the base point or points, such as the point $p''_{4,2}$ in figure 10(*a*). In order to determine the actual positions in the universal coordinate systems, the absolute position/positions of the base point/points should be decided. Two algorithms, called edge-point algorithm (EPA) and one-point algorithm (OPA), have been developed with different position assumptions. Considering the continuity of the rows, the absent center reference point in the captured image is also added as a reflected point to compute in the proposed algorithms and its position is set as the center of the two adjacent dots in the same row.

- Edge-point algorithm (EPA)

In EPA, the initial depths of the edge base points on the reflection surface are assumed to be zero. Hence, in the first loop of the algorithm, the depths of several edge points, for example in figures 11(*b*) and (*c*) the *Z* coordinate of edge reflection points $p''_{i,j}$ (except $p''_{2,4}$) corresponding to edge reflected points $r_{i,j}$ in figure 11(*a*), are set to zero. In the followed loops, the computed positions of edge base points in the previous loop are used. Here edge points are referred to the points at the end of each row, which are projected to or reflected from the edge of the weld pool surface. The assumption is based on the experimental observation that the edge reflected points of the row are on the imaging plane, but the edge reflected dots of the column may be blocked by the torch.

To calculate the positions of slope-oriented points using the slope field, the EPA-R algorithm can be used where R stands for 'row'. It uses horizontal row slopes computed in the first step and the positions of edge base points to calculate the positions of other points on the reflection surface, shown in figure 11(*b*). Since the two end points in each row can be

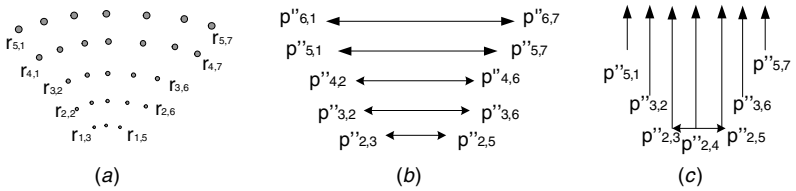


**Figure 11.** EPA algorithm illustration: (*a*) reflected dots in imaging plane; (*b*) compute with row spaces; and (*c*) compute with column slopes.

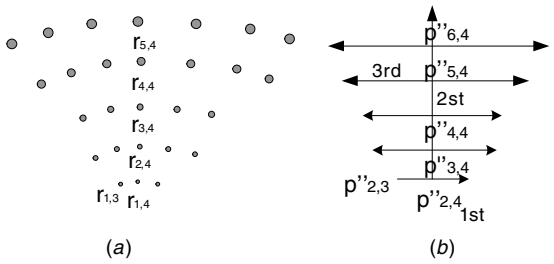


**Figure 12.** OPA algorithm illustration: (*a*) reflecting dots in imaging plane and (*b*) compute with row and column slopes.

considered edge points and be used as the base points, there are two possible new positions for each reflection point on the row. The authors use the average value of the positions as the position for the new slope-oriented point. Similarly, the column slopes may also be used and the resultant method is referred to as the EPA-C algorithm where C stands for 'Column' as shown in figure 11(*c*). In this algorithm, if the base point for the column is not an edge base point, its position should be first computed by the horizontal row slopes in the EPA-R, such as the point $p''_{2,4}$. Obviously a third method is to use the average value of the above two methods to calculate, which can be referred to as EPA-RC algorithm. In section 7.1, these methods will be tested for comparison.

- One-point algorithm (OPA)

In OPA, the depth of one edge (base) point on the reflection surface is assumed a value in a range around zero in each loop, such as from −0.5 mm to 0.5 mm. All the other reflection points are calculated based on it. For example, in figure 12(*b*) the depth of the reflection points $p''_{2,3}$ corresponding to $r_{1,3}$ is assumed to be around zero, and the position of slope-oriented reflection points in the same row is calculated using row slopes. Then the position of the center point $p''_{2,4}$ and the column slopes are used to compute the positions of other center points in different rows, such as $p''_{3,4}$, $p''_{4,4}$, $p''_{5,4}$ and $p''_{6,4}$. Finally, based on the center reflection points, all other reflection point positions can be calculated by using row slopes.

*Step* 3: reconstruction of weld pool surface using reflection points.

In the third step, a weld pool surface should be deduced depending on the slope-oriented reflection points $P''$ computed in the second step. Here a triangle-based cubic interpolation method [15] is applied to reconstruct the smooth weld pool surface, which can produce a surface from non-uniformly sampled data in the form of

$$z = f(x, y). \tag{2}$$

*Step* 4: compute the error of the interpolated surface.

In the fourth step, with the knowledge of the projected dot matrix and the surface reconstructed from the third step, the reflected points set $R'$ ($R' = \{r'_{i,j}, (i, j) \in I\}$) on the imaging plane can be re-computed and compared with the positions of the reflected points $R$ on the captured image. The differences between the actual and computed reflected points can be calculated. This error can be further mapped to the weld pool surface and denoted as 'reflection error'. If the reflection error is within the pre-specified threshold, an acceptable estimate of the weld pool surface is found and the reconstruction ends. Otherwise, this estimated surface is used as the new initial surface to continue the first step within a pre-set number of loops. If the surface reconstructed converges but the reflection error is greater than the threshold, the surface with the minimum error is chosen.

To define a meaningful error which can describe the difference between the calculated and actual reflection points on the weld pool surface, the authors propose two error measurement parameters: average reflection error ($ARE$) and maximum reflection error ($MRE$).

$$ARE = \sum_{(i,j)\in I} E_{i,j}/n, \ldots.(i, j) \in I \tag{3}$$

$$MRE = \max\{E_{i,j}, (i, j) \in I\} \tag{4}$$

where $I$ refers to the reflected image and $n$ represents the total number of reflected points on the imaging plane. $E_{i,j}$ represents the reflection error of the reflection (projected) point corresponding to the reflected point $r_{i,j}$ and it is defined as

$$E_{i,j} = \sqrt{\left(e^x_{i,j} \cdot \frac{W_p}{W_r}\right)^2 + \left(e^z_{i,j} \cdot \frac{L_p}{L_r}\right)^2} \tag{5}$$

where $e^x_{i,j}$ and $e^z_{i,j}$ are the absolute values of distance between the estimated reflected point $r'_{i,j}$ and the actual reflected point $r_{i,j}$ along the horizontal direction ($X$-axis) and vertical direction ($Z$-axis), respectively.

$$e^x_{i,j} = \left|r'^x_{i,j} - r^x_{i,j}\right|, \qquad e^z_{i,j} = \left|r'^z_{i,j} - r^z_{i,j}\right|, \quad \text{where} \quad r'_{i,j} \in R', r_{i,j} \in R. \tag{6}$$

As shown in figure 13, $W_r$ and $L_r$ represent the horizontal and vertical ranges of the reflected dots, respectively and $W_p$ and $L_p$ represent the horizontal ($X$ axis) and vertical ($Y$ axis) ranges of the corresponding projected dots on the work piece ($Z = 0$). These parameters are formulated as

$$W_p = \max\left(p^x_{m,n}\right) - \min\left(p^x_{m,n}\right), \quad L_p = \max\left(p^y_{m,n}\right) - \min\left(p^y_{m,n}\right), \quad \text{where} \quad p_{m,n} \in P \tag{7}$$

$$W_r = \max\left(r^x_{i,j}\right) - \min\left(r^x_{i,j}\right), \quad L_r = \max\left(r^z_{i,j}\right) - \min\left(r^z_{i,j}\right), \quad \text{where} \quad r_{i,j} \in R. \tag{8}$$

From equations (3)–(8), it can be seen that the defined 'reflection error' represents the estimation error of the reflection points on the weld pool surface, which is mapped from the error of reflected dots on the imaging plane. In equation (5), the first part uses the ratio $W_p/W_r$ to map the horizontal error of the reflected dot to that of the reflection dot, and in the same way the second term uses $L_p/L_r$ to get the vertical error of the reflection dot. Thus it is reasonable to use reflection error to evaluate the error of calculated reflection points on the weld pool surface.

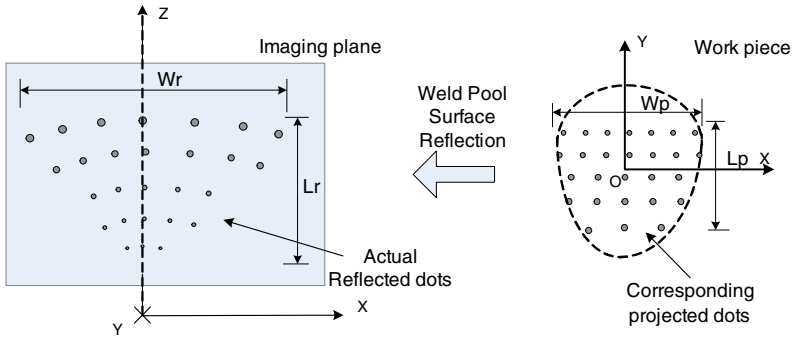


**Figure 13.** Illustration of the design of error measurement parameters.

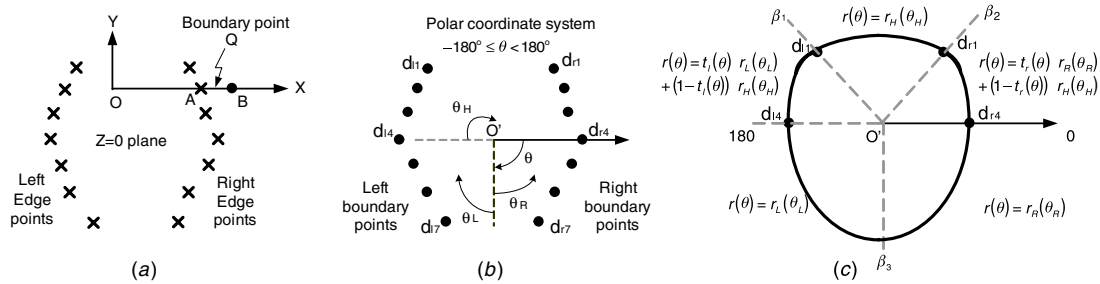


**Figure 14.** Boundary modeling illustration: (*a*) edge reflection points in universal coordinate system, (*b*) estimated boundary points in polar coordinate system and (*c*) the 2D boundary piecewise model.

## 5. Two-dimensional boundary modeling

Although the basic shape of the three-dimensional surface can be extracted from the reflected image, the boundary of the weld pool may not be directly determined. It is not guaranteed that each row of laser rays has rays to be projected exactly on the boundary. Hence, in addition to the issue how the boundary of the weld pool is mathematically described, there is also an issue how boundary points can be derived from a reflected image. While a few approaches have been proposed to describe weld pool boundaries [6, 16, 17], the authors here propose a two-dimensional piecewise boundary model which can be derived from the reflected image.

### *5.1. Determination of boundary points*

As mentioned earlier, in the system the projected dot matrix covers the whole possible weld pool surface region and all the dots located within the scope will be reflected by the specular surface. Hence, it is reasonable to believe that on the reflected images the two end points on each curved row are reflected from small neighborhoods of the two sides of the weld pool boundary, and they can be considered as 'conservative estimates of edge reflection points', which are represented as $P^e = \left\{p^e_{i,j}, (i, j) \in B\right\} \subset P$. Here $B$ is referred to the boundary and the subscripts represent the row and column numbers of the edge points.

Further, for the head of the weld pool where the boundary divides the weld pool from unmelted material, the boundary of the weld pool surface is on the $X$–$Y$ plane ($Z = 0$), i.e., on the work piece surface. For the rear of the weld pool surface in GTAW, it is also reasonable to consider that the weld pool boundary is on the $X$–$Y$ plane if no filler metal is used and the joint is a square joint with no gap as in this study. With this reasonable assumption, once the center reference point and the corresponding relationship are found, the positions of the 'conservative estimates of edge points' in set $P^e$ can be decided on the work piece. Denote the projection of $P^e$ on the work piece as $(X, Y)|_{P^e}$. These points $(X, Y)|_{P^e}$ on the work piece can be divided into left and right sides with regard to $X$–$Y$ coordinates, just as shown in figure 14(*a*). Here the experimental case in figure 6 is used as an example.

It is apparent that the boundary of the weld pool surface is not exactly passing $P^e$ but somewhere outside $(X, Y)|_{P^e}$. To illustrate how to decide better estimates of boundary points from conservative estimates $(X, Y)|_{P^e}$, figure 14 is used. As can be seen in figure 14(*a*), there is a right edge reflection point $A \subset (X, Y)|_{P^e}$ and its right neighbor point B on the $X$-axis and a actual 'boundary point' $Q$ should be located between $A$ and $B$. Suppose the position $Q(X_q)$ is a variant evenly distributed in the range $(xa, xb)$. According to the knowledge of probability, its mean and variance can be calculated as equation (9).

$$E(X_q) = (x_a + x_b)/2 \qquad D(X_q) = (x_b - x_a)^2/12. \tag{9}$$

If one chooses $X_q = k$ $(xa < k < xb)$, the mean square error (MSE) is

$$\mathrm{MSE} = E[(X_q - k)^2] = \frac{1}{(x_b - x_a)} \cdot \int_{x_a}^{x_b} (X_q - k)^2 \, \mathrm{d}X_q. \tag{10}$$

In order to minimize the MSE, the requirement of equation (11) should be met:

$$\frac{\partial \mathrm{MSE}}{\partial k} = 0. \tag{11}$$

From equations (10) and (11), the optimal $k$ is calculated as

$$k = (x_a + x_b)/2 = E(X_q). \tag{12}$$

Hence, the optimal estimation of boundary point $Q$ is the middle point of points $A$ and $B$. Based on the positions of edge reflection points $P^e$ in the $X$–$Y$ plane, the positions of boundary points are determined, which form the point set $D$ as shown in figure 14($b$).

### 5.2. Weld pool boundary fitting

In figure 14($b$) only the positions of the boundary points on two sides of the weld pool are known. Divide the weld pool boundary points in the set $D$ into left and right parts. The left points are marked $d_{l1}, d_{l2}...d_{li}...d_{l7}$ and the right points are marked $d_{r1}, d_{r2}...d_{ri}...d_{r7}$. A polar coordinate system is set up for the weld pool boundary modeling and the origin point $O'$ is chosen as the middle point of the widest boundary point pairs in a row, such as the pair of $d_{l4}$ and $d_{r4}$ in figure 14($b$). The direction of angle $\theta$ in the polar coordinate system is clockwise as shown in the figure. The universal coordinates of all the boundary points in the set $D$ should be converted into established polar coordinates $(r, \theta)$ and the angle parameter $\theta$ ranges from $-180^\circ$ to $180^\circ$. Then the pool boundary can be modeled by relating the radius $r$ to the angle $\theta$ in the polar coordinate system.

In the study, the weld pool boundary is segmented into three parts: left, right and head. The head part is introduced to fit the actual size of weld pool surface and make the left and right parts merge smoothly. The following polar coordinate model is used to describe the three parts of the weld pool boundary.

$$r(\theta) = \omega_0 + \sum_{i=1}^{p} (\omega_i \cdot \theta^p). \tag{13}$$

Here $p$ is the order of the fitted equation. Usually the higher the order is, the more precise the model is. Considering the balance between computational complexity and accuracy, third order is selected in the model.

The available boundary points in set $D$ can be assigned into three sets used for left, right and head segment boundary fitting. They are presented as point sets $L$, $R$ and $H$.

$$\begin{aligned} L &= \left\{ \left(l_i, \theta_{l_i}\right) \middle| 90^\circ \leqslant \theta_{l_i} \leqslant 180^\circ \text{ or } -180^\circ < \theta_{l_i} \right. \\ &\quad \left. \leqslant -90^\circ, \left(l_i, \theta_{l_i}\right) \in D \right\} \\ R &= \left\{ \left(r_i, \theta_{r_i}\right) \middle| -90^\circ < \theta_{r_i} < 90^\circ, \left(r_i, \theta_{r_i}\right) \in D \right\} \\ H &= \left\{ \left(h_i, \theta_{h_i}\right) \middle| -180^\circ \leqslant \theta_{h_i} \leqslant 0^\circ, \left(h_i, \theta_{h_i}\right) \in D \right\}. \end{aligned} \tag{14}$$

In order to make the model continued in their segments, the angle parameter $\theta$ of boundary points in equation (14) is replaced by $\theta_L$, $\theta_R$ and $\theta_H$, respectively, for modeling the different parts. From figure 14($b$), the relationships between them are derived.

$$\begin{cases} \theta_L = \begin{cases} \theta - 90^\circ \text{ when } 90^\circ \leqslant \theta \leqslant 180^\circ \\ \theta + 270^\circ \text{ when } -180^\circ < \theta \leqslant -90^\circ \end{cases} & \text{in } L \\ \theta_R = 90^\circ - \theta & \text{in } R \\ \theta_H = \theta + 180^\circ & \text{in } H. \end{cases} \tag{15}$$

Then the three segments of the weld pool boundary are modeled as shown in equation (16).

$$\begin{cases} r_L(\theta_L) = \omega_{L0} + \sum_{i=1}^{p} \left(\omega_{Li} \cdot \theta_L^p\right) \\ \quad = (\omega_{L0} \quad \omega_{L1} \quad \omega_{L2} \quad \omega_{L3}) \times \left(1 \quad \theta_L \quad \theta_L^2 \quad \theta_L^3\right)^{\mathrm{T}} \\ r_R(\theta_R) = \omega_{R0} + \sum_{i=1}^{p} \left(\omega_{Ri} \cdot \theta_R^p\right) \\ \quad = (\omega_{R0} \quad \omega_{R1} \quad \omega_{R2} \quad \omega_{R3}) \times \left(1 \quad \theta_R \quad \theta_R^2 \quad \theta_R^3\right)^{\mathrm{T}} \\ r_H(\theta_H) = \omega_{H0} + \sum_{i=1}^{p} \left(\omega_{Hi} \cdot \theta_H^p\right) \\ \quad = (\omega_{H0} \quad \omega_{H1} \quad \omega_{H2} \quad \omega_{H3}) \times \left(1 \quad \theta_H \quad \theta_H^2 \quad \theta_H^3\right)^{\mathrm{T}}. \end{cases} \tag{16}$$

To find the proper coefficients for the above model, the least-squares method is chosen to estimate them by applying the boundary points in sets $L$, $R$ and $H$, respectively. The criteria used for determination can be expressed as

$$\begin{aligned} &\omega_{Li}(i = 0, 1, 2, 3) : \min \sum_{j=1}^{N_l} (l_j - r_L(\theta_{Lj}))^2 \\ &= \min \sum_{j=1}^{N_l} \left[ l_j - (\omega_{L0} \quad \omega_{L1} \quad \omega_{L2} \quad \omega_{L3}) \right. \\ &\quad \left. \times \left(1 \quad \theta_{Lj} \quad \theta_{Lj}^2 \quad \theta_{Lj}^3\right)^{\mathrm{T}} \right]^2 \\ &\omega_{Ri}(i = 0, 1, 2, 3) : \min \sum_{j=1}^{N_r} (r_j - r_R(\theta_{Rj}))^2 \\ &= \min \sum_{j=1}^{N_r} \left[ r_j - (\omega_{R0} \quad \omega_{R1} \quad \omega_{R2} \quad \omega_{R3}) \right. \\ &\quad \left. \times \left(1 \quad \theta_{Rj} \quad \theta_{Rj}^2 \quad \theta_{Rj}^3\right)^{\mathrm{T}} \right]^2 \\ &\omega_{Hi}(i = 0, 1, 2, 3) : \min \sum_{j=1}^{N_h} (h_j - r_H(\theta_{Lj}))^2 \\ &= \min \sum_{j=1}^{N_h} \left[ h_j - (\omega_{H0} \quad \omega_{H1} \quad \omega_{H2} \quad \omega_{H3}) \right. \\ &\quad \left. \times \left(1 \quad \theta_{Hj} \quad \theta_{Hj}^2 \quad \theta_{Hj}^3\right)^{\mathrm{T}} \right]^2 \end{aligned} \tag{17}$$

where $N_l$, $N_r$ and $N_h$ are the number of points in sets $L$, $R$ and $H$, respectively. By using the standard least-squares method the parameters $\omega_{Li}$, $\omega_{Ri}$ and $\omega_{Hi}$ $(1 \leqslant i \leqslant 3)$ can be solved.

After solving equation (17), the equations for the three segments of the weld pool boundary are gained, but they are not smoothly connected. Therefore in the proposed 2D piecewise boundary model, the boundary is further divided into five parts by adding two transition areas between the head segment and the other two segments, which is shown in figure 14($c$). Then the whole boundary of the weld pool $r(\theta)$ is calculated using the following equations:

$$\begin{aligned} &r(\theta) = r_H(\theta_H) = r_H(\theta + 180^\circ) && \beta_1 \leqslant \theta \leqslant \beta_2 \\ &r(\theta) = t_l(\theta) \cdot r_L(\theta_L) + (1 - t_l(\theta)) \cdot r_H(\theta_H) \\ &\quad = t_l(\theta) \cdot r_L(\theta + 270^\circ) + (1 - t_l(\theta)) \cdot r_H(\theta + 180^\circ) \\ &\qquad\qquad && -180 < \theta < \beta_1 \\ &r(\theta) = r_L(\theta_L) = r_L(\theta - 90^\circ) && \beta_3 \leqslant \theta \leqslant 180 \\ &r(\theta) = t_r(\theta) \cdot r_R(\theta_R) + (1 - t_r(\theta)) \cdot r_H(\theta_H) \\ &\quad = t_r(\theta) \cdot r_R(90^\circ - \theta) + (1 - t_r(\theta)) \cdot r_H(\theta + 180^\circ) \\ &\qquad\qquad && \beta_2 < \theta < 0 \\ &r(\theta) = r_R(\theta_R) = r_R(90^\circ - \theta) && 0 \leqslant \theta < \beta_3. \end{aligned} \tag{18}$$

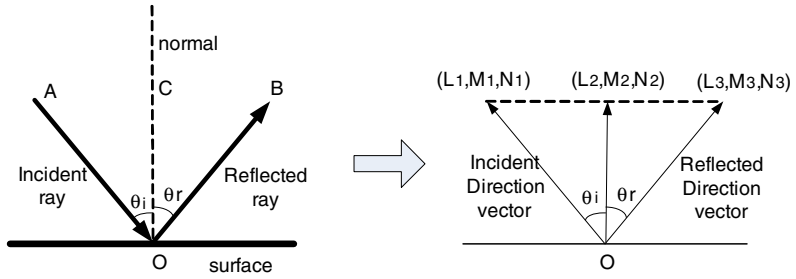


**Figure 15.** Illustration of reflected line computation.

where $t_l(\theta)$ and $t_r(\theta)$ are the weights, which are defined as

$$\begin{aligned} t_l(\theta) &= (\beta_1 - \theta)/(\beta_1 + 180^\circ) \qquad -180 < \theta < \beta_1 \\ t_r(\theta) &= 1 - \theta/\beta_2 \qquad\qquad\qquad \beta_2 < \theta < 0 \end{aligned} \tag{19}$$

where $\beta_1$, $\beta_2$, $0^\circ$, $180^\circ$ and $\beta_3$ are the boundaries for the segments. $\beta_1$ is defined as the largest angle of the boundary point among $(-180^\circ, -90^\circ)$ in the set L; $\beta_2$ is defined as the smallest angle of the point in the set $R$; and $\beta_3$ is the intersection angle of the left segment $r_L(\theta_L)$ and the right segment $r_R(\theta_R)$, which is the rear angle of the weld pool.

## 6. Reconstruction implementation

MATLAB is used to implement the proposed slope-based reconstruction algorithms. During the implementation process of the algorithms, the geometrical representation of objects, such as 3D lines, planes and surfaces, and the realization of the reflection law are the most important parts. Here some expressions, which are used for reconstruction implementation, are discussed below.

### 6.1. Incident line

For the projected dot matrix rays, the incident laser ray at row $i$ and column $j$ can be described by its direction vector and the coordinates of the laser diode point, which is shown in equation (20).

$$\begin{cases} x_{i,j} = x_0 + px_{i,j} \cdot t \\ y_{i,j} = y_0 + py_{i,j} \cdot t \\ z_{i,j} = z_0 + pz_{i,j} \cdot t. \end{cases} \tag{20}$$

Here $[x_0, y_0, z_0]$ represents the universal coordinates of the laser diode and $[px_{i,j}, py_{i,j}, pz_{i,j}]$ is the direction vector of the laser beam at row $i$ and column $j$. The parameter $t$ is an independent variable. Since the inter-beam angle (the angle between adjacent laser rays) of the laser diode with the dot matrix pattern is known, the direction vectors of the laser beam can be easily derived.

### 6.2. Normal line

Suppose $S$ is a surface with equation $z = f(x, y)$ (or $F(x, y, z) = z - f(x, y) = 0$) and $P = (x_p, y_p, z_p)$ is a point on $S$. Then the direction of the normal line at point $P$ can be expressed as follows:

$$\begin{cases} F_x(x_p, y_p, z_p) = f_x(x_p, y_p) \\ F_y(x_p, y_p, z_p) = f_y(x_p, y_p) \\ F_z(x_p, y_p, z_p) = -1 \end{cases}. \tag{21}$$

If the surface equation is not known and the incident line and its reflected line are known, the normal line is the angle bisector of the angle formed by incident and reflected lines and it can thus be computed.

### 6.3. Reflected line

The reflected lines were calculated based on the law of reflection, which states that the incident angle of a light beam is equal to the angle of reflection. Figure 15 illustrates this concept where $\theta_i$ is equal to $\theta_r$. Here incident line AO and normal OC are known, and the reflected line OB is unknown.

Based on the knowledge of geometry, it is known if the length of segment AO is equal to the length of OB, then the center point of AB is on the normal. Suppose the direction vector $(L_1, M_1, N_1)$ of the incident ray OA and the direction vector $(L_3, M_3, N_3)$ of the reflected ray OB are both normalized and their lengths are equal to 1, and the direction vector of normal line OC is $(L_2, M_2, N_2)$.

$$\begin{cases} L_2 \cdot k = (L_1 + L_3)/2 \\ M_2 \cdot k = (M_1 + M_3)/2 \\ N_2 \cdot k = (N_1 + N_3)/2 \\ \sqrt{L_3^2 + M_3^2 + N_3^2} = 1 \end{cases} \tag{22}$$

where $k$ is a positive variable and $(L_2 \times k, N_2 \times k, M_2 \times k)$ represents the position of the point C. Solving the above equations gives the reflected direction

$$\begin{cases} L_3 = 2 \cdot k \cdot L_2 - L_1 \\ M_3 = 2 \cdot k \cdot M_2 - M_1 \\ N_3 = 2 \cdot k \cdot N_2 - N_1 \\ k = (L_1 \cdot L_2 + M_1 \cdot M_2 + N_1 \cdot N_2) \big/ \left(L_2^2 + M_2^2 + N_2^2\right). \end{cases} \tag{23}$$

Since the reflected direction vector can be calculated with incident and normal directions, the reflected line can be easily expressed using the direction vector and any one point on it, just as the incident line. Furthermore if incident and reflected lines are known, the normal can be computed similarly.

## 7. Results and discussion

Proposed slope-based surface reconstruction algorithms rebuild the middle weld pool surface area which reflects the projected laser dots onto the imaging plane, and the established two-dimensional boundary model helps us to find the weld pool boundary. Combined with information on the middle part and the boundary part, the whole weld pool surface can be reconstructed by interpolation again. That means the optimal

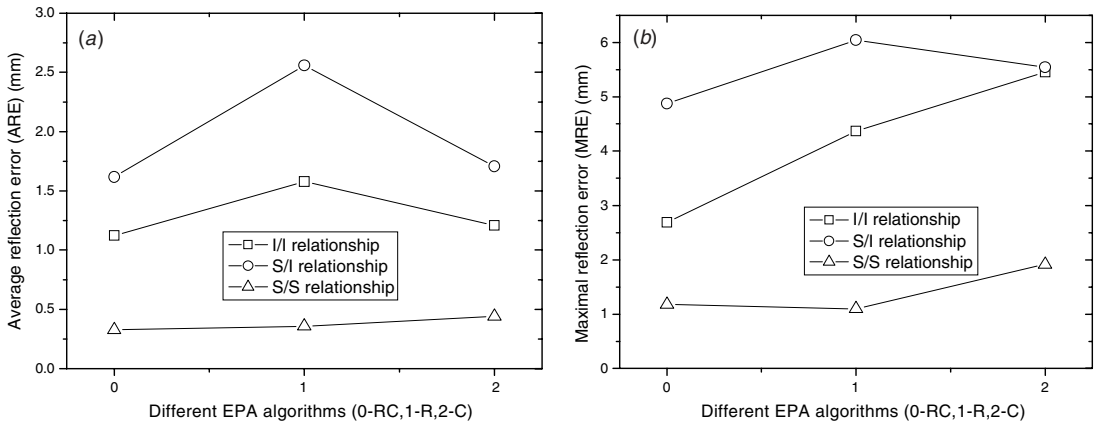


**Figure 16.** Results of EPA algorithms: (*a*) average reflection error and (*b*) maximal reflection error. In the figures, '0' represents algorithm EPA-RC; '1' represents algorithm EPA-R; and '2' represents algorithm EPA-C.

estimated reflection points and the modeled boundary points can be used together to do interpolations so as to reconstruct the whole weld pool surface.

A reflected image captured during the experiment is used to test the slope-based reconstruction method, which is shown in figure 6(*a*). The reflected dots extracted using image processing algorithms are shown in figure 6(*b*). Two algorithms (EPA and OPA) are tested in our study using the reflected image above, and their results are shown. It can be seen from figure 8 that the purpose of setting the error threshold in step 4 is to expedite the algorithm; thus it is not used in the experiments here in order to find the optimal result within pre-set loops.

### *7.1. EPA algorithm result*

Since the actual shape of the weld pool surface cannot be measured directly, the error of the reconstructed surface is measured by the two indirect error measurement parameters proposed in section 4: average reflection error (ARE) and maximum reflection error (MRE). For the reflected image in figure 6(*a*), some related dimension parameters in equation (3) are calculated as follows:

$W_r = 40.17$ mm, $L_r = 47.25$ mm;
$W_p = 6.15$ mm, $L_p = 4.52$ mm (for I/I and S/I corresponding relationships);
$W_p = 6.67$ mm, $L_p = 5.41$ mm (for S/S corresponding relationship).

As can be seen, the values of $W_p$ and $L_p$ change a little for different row corresponding relationships. These results are the same for the OPA algorithm.

Figure 16 shows the experimental results of the EPA algorithms under different situations, and here 100 loops are tried for each situation. The horizontal axis represents different methods used to compute the reflection points: 0 for EPA-RC, 1 for EPA-R and 2 for EPA-C. Three possible corresponding relationships discussed in section 2.2 are all considered in order to improve the veracity and compatibility of the algorithms. Here the symbol 'S' represents sequential and 'I' represents inverse, and the first letter in front of '/' represents column corresponding relationship and the second after '/' represents row corresponding relationship.

As can be seen in figure 16, EPA algorithms can effectively differentiate different corresponding relationships and the S/S corresponding relationship can achieve better results. Comparing different ways to use the slopes in figure 16(*a*), the performance of EPA-RC is a little better than the other two, and the minimal average reflection error (ARE) is 0.33 mm. The minimal MRE 1.10 mm is achieved by EPA-R. Here the ARE is considered as the primary standard to get the interpolated optimal weld pool surface, which is shown in figure 17. It is a deformed convex surface and most of the weld pool surface is reconstructed by the algorithm.

In figure 18, the positions of actual reflection points and computed reflected points using an interpolated surface by the EPA algorithm are shown. As can be seen, their difference or the error is not small and especially large in the neighborhood of the edge. It should be noted that the absent center reference point in the captured image is also shown as a reflected point, and its position is set at the center of the adjacent dots in the same row.

### *7.2. OPA algorithm result*

In the OPA algorithm, the depth (height) of one edge (base) reflection point on the work piece plane, which corresponds to the point in the left-down corner on the image, is set and its *X*–*Y* coordinates are decided accordingly on the incident ray. Then the other reflection points are calculated based on it. Figure 19 shows the minimal average reflection error (ARE) and maximum reflection error (MRE) of the OPA algorithm under different situations and 100 loops are tried for each situation. The height of the base edge point is changed from $-0.5$ mm to 0.5 mm, which is reasonable for practical applications.

In figure 19 the performances of different corresponding relationships can be easily differentiated and the S/S corresponding relationship gives a better result, which also proved the validity of the OPA algorithm. For an average reflection error (ARE), the minimal value 0.17 mm is achieved when the height is 0 mm with the S/S relationship. In

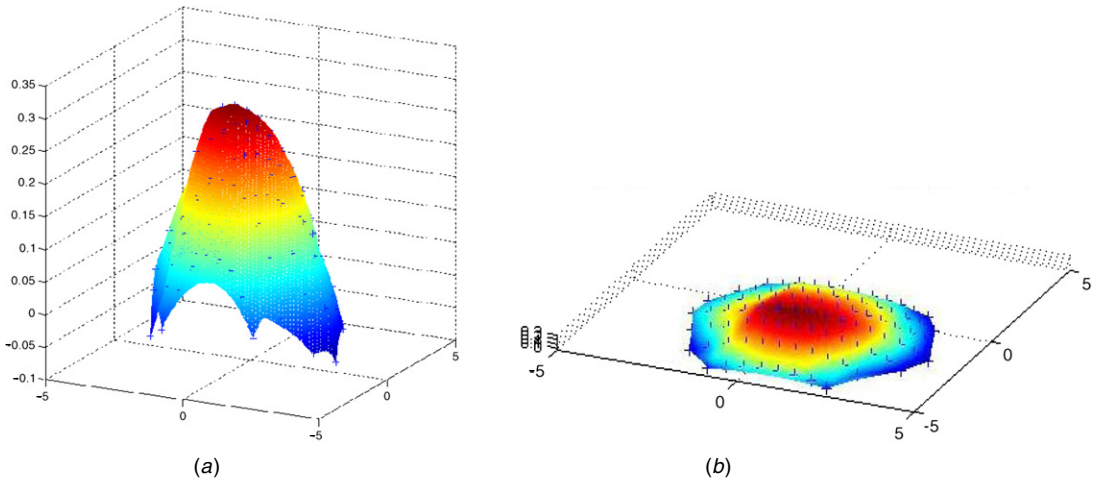


**Figure 17.** Optimal weld pool surface reconstructed by EPA algorithms: (*a*) close view (*Z* axis is amplified) and (*b*) view with equal axes.

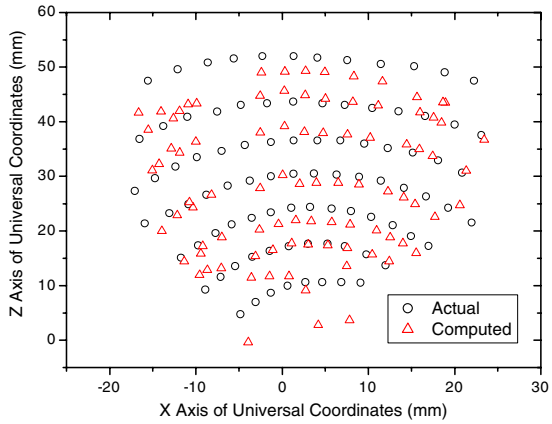


**Figure 18.** Computed and actual reflection points compared on the imaging plane (EPA).

figure 19(*a*), there is only a little difference among the results under different assumptions, and this may be caused by the small difference between assumed depths (only 0.1 mm). Figure 19(*b*) also verifies that the S/S relationship has the better performance for maximal reflection error (MRE), and the minimal MRE is 0.87 mm when height is −0.2 mm.

Here ARE is taken as the primary standard, and the optimal interpolated weld pool surface with marked reflection points is shown in figure 20. As can be seen, the reconstructed surface is a shallow smooth convex surface and is rebuilt in most parts.

In figure 20, the positions of actual reflection points and computed reflected points using an optimal interpolated surface are shown. The difference between them is small in the middle part, but larger for the edge points because the slopes of the edge points are not precise enough for the interpolation method.

Moreover, the average reflection error of inside points (ARE-I) in the middle part and the maximum reflection error of inside points (MRE-I) are also defined and evaluated in figure 22 by eliminating the influence of the edge points' large errors caused by the interpolation method. In this example, the edge points refer to the reflection points corresponding to the reflected points in the 1st and 7th rows and on both ends of each row in figure 21. The optimal interpolated weld pool surface is also achieved by using the *S*/*S* corresponding relationship with depth 0 and the same result is shown in figure 20. As can be seen, the minimal average reflection error of inside points (ARE-I) is 0.08 mm, which is much less than the minimal ARE for all the reflected points in figure 19(*a*).

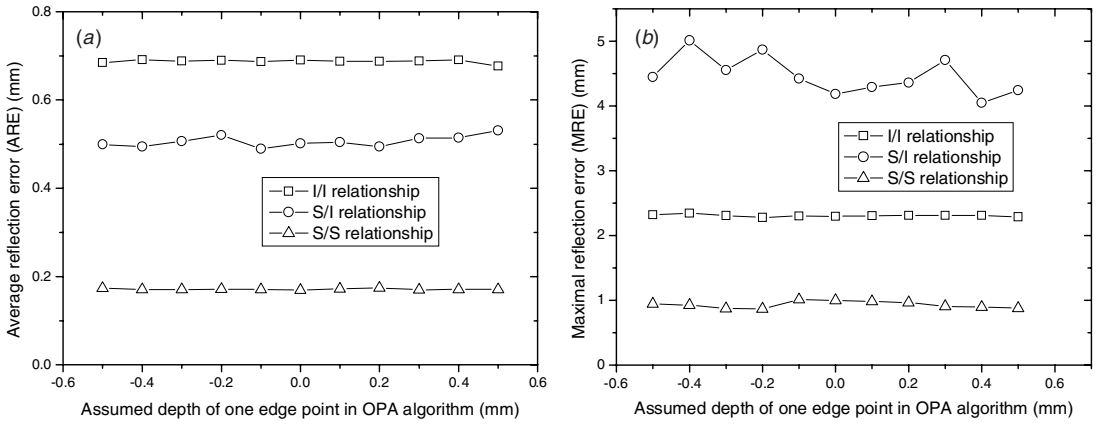


**Figure 19.** Results of OPA algorithm: (*a*) average reflection error and (*b*) maximal reflection error.

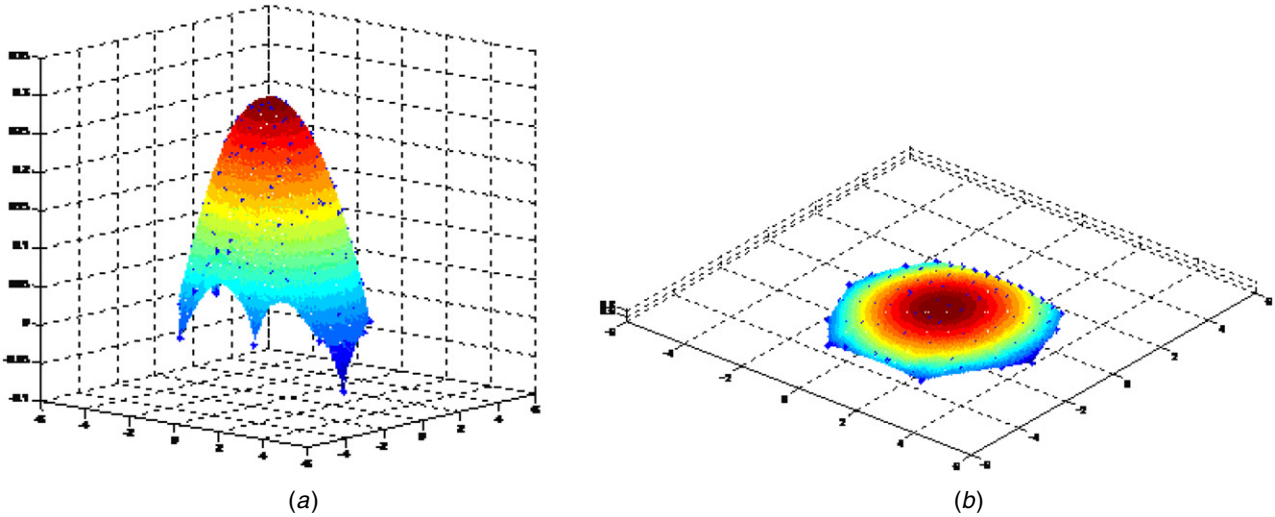


**Figure 20.** Optimal interpolated weld pool surface reconstructed by OPA algorithm: (*a*) close view (*Z* axis is amplified) and (*b*) view with equal axes.

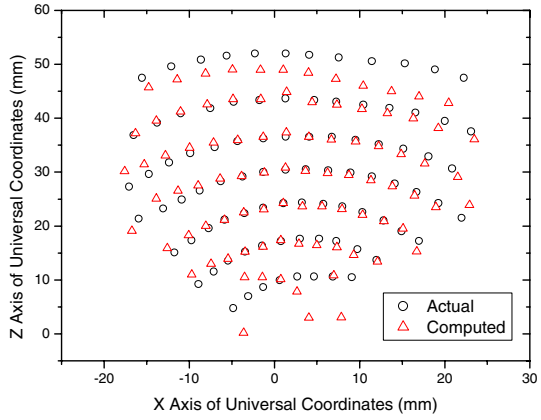


**Figure 21.** Computed and actual reflection points compared on the imaging plane (OPA).

The minimal MRE-I, 0.22 mm, is also much less than the result in figure 19(*b*).

### *7.3. Algorithm comparison*

The above results show EPA and OPA algorithms can achieve similar results in reconstructing the weld pool surface. For the studied reflected image in figure 6, the reconstructed weld pool surfaces by the two algorithms are both convex, which agrees with the eye direct observation result. The heights of the weld pool surfaces are both around 0.3 mm.

According to the errors of the algorithms, it is obvious the OPA algorithm has a better performance than the EPA. The minimal ARE and MRE of the OPA algorithm are smaller and the interpolated weld pool surface is smoother than the results of the EPA algorithm. The possible reason is that the assumption of one edge point position in the OPA algorithm is more reasonable.

### *7.4. Boundary models and the reconstructed results*

By using a slope-based surface reconstruction method, the interpolated optimal weld pool surfaces are reconstructed in figures 17 and 20. As can be seen, only the middle area of the weld pool surface covered by the dot matrix is rebuilt.

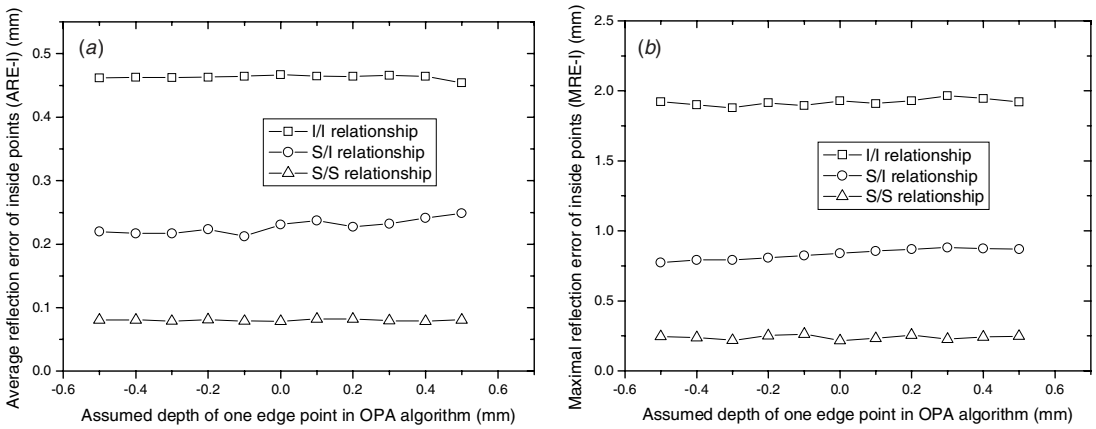


**Figure 22.** Results of the OPA algorithm by different parameters: (*a*) ARE-I and (*b*) MRE-I.

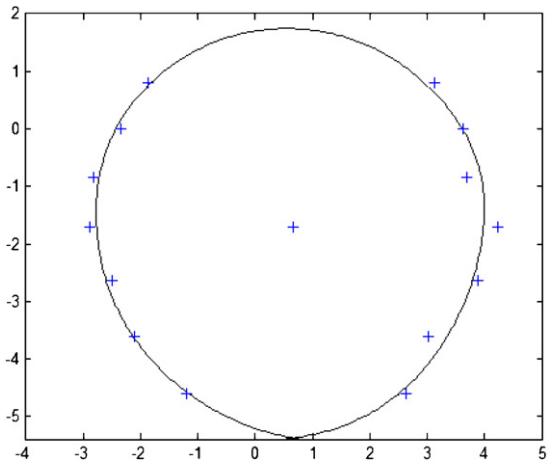

**Figure 23.** Fitted two-dimensional weld pool boundary model (on $Z = 0$ plane).

The 2D boundary model described in section 5 is, thus, used to find the boundary of the weld pool surface.

Based on the results of the slope-based reconstruction method, the S/S corresponding relationship and the reflected dots on the imaging plane are used to find the boundary points. Figure 23 shows the boundary points of the pool surface on the work piece ($Z = 0$ plane) and the fitted two-dimensional (2D) boundary by using the proposed modeling method. The center point is the origin of the used polar coordinate system. The shape of the modeled 2D boundary is similar to those shown in figure 1. Because the welding speed is slow (3 mm $s^{-1}$), the difference between the width (6.73 mm) and length (7.12 mm) is small and the 2D shape of weld pool is circular, which can be verified by the measurement result after the experiment.

In figure 24, the new whole interpolated weld pool surfaces are reconstructed by using both the boundary model and the optimal surfaces computed by the EPA and OPA algorithms. As can be seen, the two reconstructed surfaces are similar and they are both convex with nearly the same

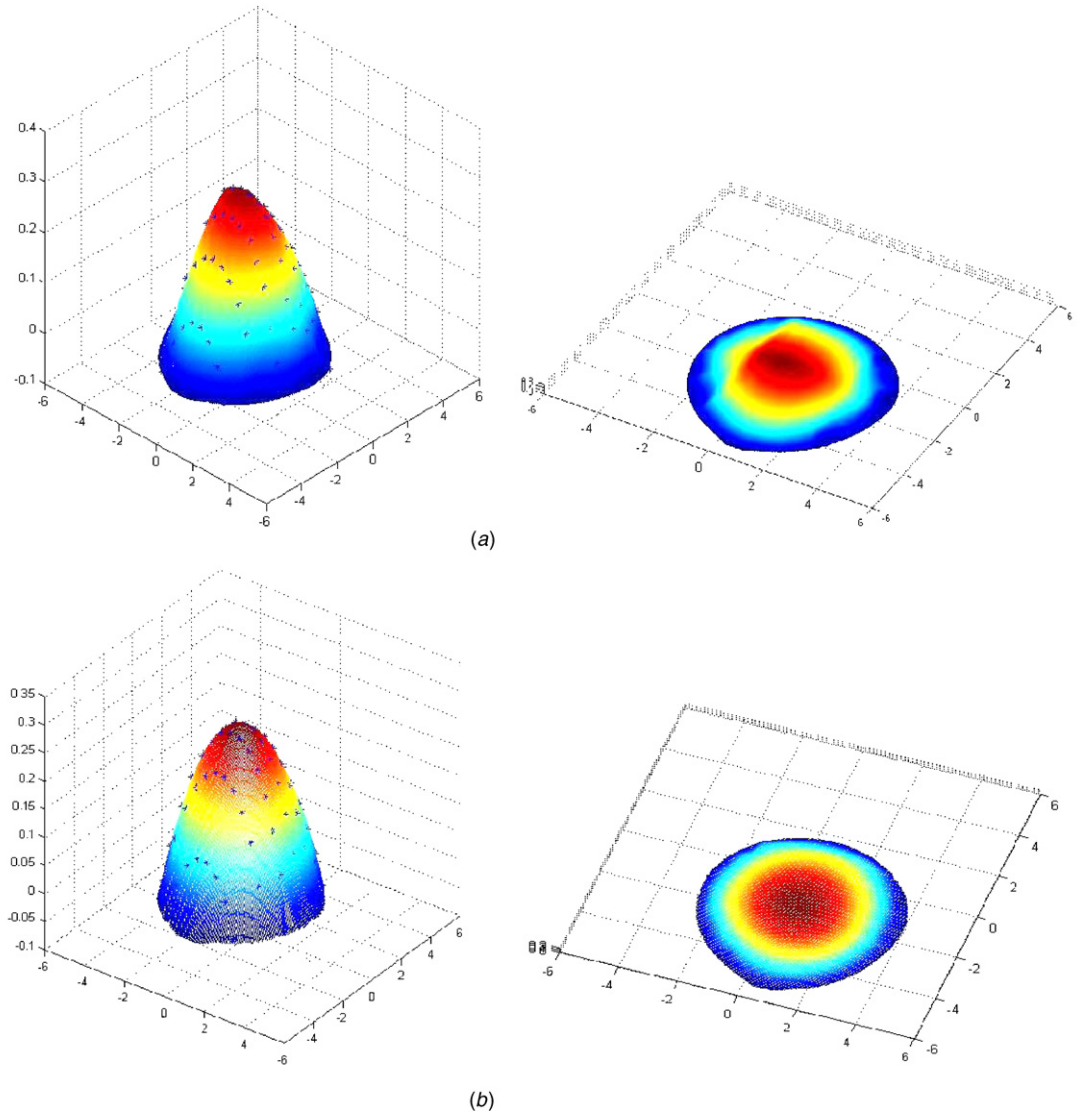

**Figure 24.** Reconstructed whole weld pool surface: (*a*) weld pool surface using the EPA algorithm and 2D boundary model and (*b*) weld pool surface using the OPA algorithm and 2D boundary model.

height. This is related to the properties of the welded work piece—mild steel. The heights of the surfaces are 0.31 mm and 0.30 mm, respectively, in figures 24(*a*) and (*b*). The surface using the OPA algorithm is smoother than the one using the EPA, which meets the practical situation of the weld pool surface.

However, in the reconstructed pool surfaces, there is no concave part inside the weld pool surface under the torch, which should appear in the practical case because of the arc pressure. The possible explanation is that the concave part in the weld pool surface is very small due to the low welding current (75 A) and there are no laser dots projected onto it. As shown in the results, although the optimal results only have small errors, obvious differences of the reflected images can still be seen in figures 18 and 21. Since it is a sensing system for small objects, there are many factors in each step of the scheme that may bring errors, such as the measurement, image processing, the surface interpolation and boundary modeling process.

## 8. Conclusion

This paper focuses on the development of algorithms for reconstructing a three-dimensional weld pool surface based on the processed reflected image, which is obtained by the proposed new sensing system. The authors found the following.

- The proposed use of the laser reflection and dot-matrix pattern and the proposed image processing algorithms form an effective system to acquire the data which can be used to compute the specular weld pool surface based on the reflection law.
- The two algorithms (OPA and EPA) can effectively use slope field information to compute the reflection points based on the assumptions of different edge point positions and interpolate the weld pool surface using these points. Some error evaluation parameters related to the difference between captured and computed reflected dot positions are proposed to find the optimal result. The depth information of the weld pool surface can be acquired by the algorithms.
- In the proposed algorithms, experiments show the OPA algorithm has better performance than the EPA algorithm. It has smaller errors and produces smoother weld pool surface. This is because of its more reasonable assumption.
- The proposed 2D boundary model uses the reliable boundary points to fit three different parts of the weld pool surface boundary in the polar coordinate system. The synthesized boundary successfully describes the 2D shape of the weld pool and provides important complementary information to rebuild the whole weld pool surface. The width and length parameters can also be extracted by the modeling method.
- This off-line reconstruction method is also valuable for real-time applications. Through appropriate simplifications, it is possible that revisions of the algorithms can be applied to estimate the 3D parameters of the weld pool surface and be used in weld pool surface control.

## Acknowledgments

This research is funded by the National Science Foundation under grant DMI-0527889 ‘Sensors: Measurement of Dynamic Weld Pool Surface’. Hongsheng Song also thanks the University of Kentucky Graduate School for the financial support through the Kentucky Opportunity Scholarship.

## References

[1] Saeed G M 2005 3 dimensional measurement of specular surfaces and its application in welding process *PhD Thesis* University of Kentucky

[2] Guu A C and Rokhlin S 1989 Computerized radiographic weld penetration control with feedback on weld pool depression *Mater. Eval.* **47** 1204–10

[3] Siores E 1988 Development of a realtime ultrasonic sensing system for automated and robotic welding *PhD Thesis* Brunel University

[4] Groenwald R A, Mathieson T A, Kedzior C T and Gaid I N C 1979 Acoustic emission weld monitor system—data acquisition and investigation *US Army Tank-Automotive Research and Development Command Report ADA085–518*, October 1979

[5] Kovacevic R, Zhang Y M and Ruan S 1995 Sensing and control of weld pool geometry for automated GTA welding *ASME J. Eng. Indust.* **117** 210–22

[6] Kovacevic R and Zhang Y M 1997 Real-time image processing for monitoring of free weld pool surface *ASME J. Manuf. Sci. Eng.* **119** 161–9

[7] Mnich C, Al-Bayat F, Debrunner C, Steele J and Vincent T 2004 *In situ* weld pool measurement using stereovision *ASME, Proc. 2004, Japan–USA Symp. on Flexible Automation (Denver, CO, 19–21 July, 2004)*

[8] Yoo C D and Lee J 3D measurement of weld pool using biprism stereo vision sensor, http://joining1.kaist.ac.kr/research/vision.htm, Seoul National University

[9] Zhang Y M, Song H S and Saeed G 2006 Observation of a dynamic specular weld pool surface *Meas. Sci. Technol.* **17** L9–L12

[10] Song H, Saeed G and Zhang Y M 2006 Observation of dynamic specular weld pool surface *Proc. 2006 ISFA (Int. Symp. Flexible Automation), 0252-b(S) (Osaka, Japan, 10–12 July , 2006)* pp 661–2

[11] Song H and Zhang Y 2007 An image processing scheme for measurement of specular weld pool surface *Proc. 2nd IEEE Conf. Industrial Electronics and Applications (ICIEA 2007) (Harbin, China 23–25 May, 2007)*

[12] Snyder W E and Qi H 2004 *Machine Vision* (Cambridge: Cambridge University Press) ISBN 052183046X

[13] Gonzalez R C and Woods R E 2002 *Digital Image Processing* 2nd edn (Englewoods Cliff, NJ: Prentice Hall)

[14] Lou M 2003 Computation of weld pool surface from specular reflection and optical flow *Master Thesis* University of Kentucky

[15] Barber C B, Dobkin D P and Huhdanpaa H T 1996 The Quickhull algorithm for convex hulls *ACM Trans. Math. Softw.* **22** 469–83

[16] Kovacevic R and Zhang Y M 1995 Machine vision recognition of weld pool in GTAW *Proc. Inst. Mech. Eng. B: J. Eng. Manuf.* **208** 141–52

[17] Kovacevic R, Zhang Y M and Li L 1996 Monitoring of weld penetration based on weld pool geometrical appearance *Welding J.* **75** 317s–29s